Integrated Microelectromechanical Gyroscopes

Huikai Xie[1] and Gary K. Fedder[2]

Abstract: Microelectromechanical (MEMS) gyroscopes have wide-ranging applications including automotive and consumer electronics markets. Among them, complementary metal-oxide semiconductor-compatible MEMS gyroscopes enable integration of signal conditioning circuitry, multiaxis integration, small size, and low cost. This paper reviews various designs and fabrication processes for integrated MEMS gyroscopes and compares their performance. Operational principles and design issues of MEMS vibratory gyroscopes are also addressed.

Introduction

Microelectromechanical system (MEMS) gyroscopes are widely believed to be a low-cost solution for medium-performance requirements. The automotive market is demanding low-cost gyroscopes for sensing yaw rate to compensate braking and suspension systems for driving security and comfort. Consumer electronic markets desire handheld products with motion stability control. Inspired by the successful commercialization of microaccelerometers (Payne et al. 1995), MEMS researchers in academia and industry have studied gyroscopes extensively in the past ten years. In fact, Robert Bosch Corporation started to sell MEMS gyroscopes for dynamic control of automobiles a few years ago (Lutz et al. 1997). Silicon Sensing Systems (SSS) is providing MEMS gyroscopes for Segway Human Transporters (Hombersley 2002). Analog Devices, Inc. (ADI) just launched its first generation integrated MEMS gyroscope (Wisniowski 2002). The ADI device is the first commercially available MEMS gyroscope to be monolithically integrated with circuits. In this paper, such monolithic integration is defined as an "integrated MEMS gyroscope." Other MEMS gyroscopes are made in an assembled multichip solution, with separate micromechanical and electronics chips.

A brief outline of MEMS gyroscopes not integrated with electronics indicates the breadth of operating principles and fabrication processes that have been explored. Draper Lab, proposed the first silicon micromachined vibratory-rate gyroscope in 1991 (Greiff et al. 1991). The mechanism was a suspended tuning-fork structure driven into resonance by electrostatic actuation. After that, various mechanisms, such as vibrating beams or rings (Maenaka et al. 1995; Putty and Najafi 1994), tuning forks (Bernstein et al. 1993), spinning disks (Shearwood et al. 1995), and surface-acoustic waves (Kurosawa et al. 1998), were investigated

for use in gyroscopes. Spinning gyroscopes have contact bearings, which pose a reliability problem. Surface-acoustic and fiber-optic gyroscopes require substantial process and materials development and integration. Among the various kinds of mechanisms, the suspended vibratory type, including tuning forks and vibrating beams or rings, is dominant because it is more suitable for batch fabrication in current micromachining processes.

For example, Delphi used electroplated metal ring structures (Sparks et al. 1999), University of Michigan explored both polysilicon and single-crystal silicon ring structures (Ayazi and Najafi 2001; He and Najafi 2002), and SSS has a metal ring in their product (Hopkin 1994). The majority of MEMS gyroscopes use vibrating beam structures, such as polysilicon structures by ADI (Geen et al. 2002), Bosch (Lutz et al. 1997; Funk et al. 1999), Murata (Tanaka et al. 1995), Samsung (Park et al. 1997) and UC-Berkeley (Clark et al. 1996; Juneau et al. 1997), single-crystal silicon structures by Carnegie Mellon (Xie and Fedder 2002a), JPL (Tang et al. 1997), Murata (Mochida et al. 1999), and Samsung (Park et al. 1999), and compound aluminum/silicon oxide structures by Carnegie Mellon (Xie and Fedder 2001; Luo 2002).

Silicon-based MEMS processes may be categorized into bulk micromachining and surface micromachining. A large mass is desired for a gyroscope because thermomechanical noise (Brownian noise) is inversely proportional to mass. Generally speaking, bulk-micromachined gyroscopes have large mass and relatively large readout capacitance or piezoresistive readout. Therefore, most bulk-micromachined gyroscopes do not incorporate on-chip readout electronics, but instead require wire bonding to separate electronic readout chips (a "two-chip" solution). Two-chip gyroscopes have a relatively large package size that restricts their applications in consumer electronics regardless of price. In contrast, surface-micromachining gyroscopes have small mass and relatively small readout capacitance. However, the sensors and readout electronics are usually integrated on a single chip, to reduce parasitic capacitance. Some work has been conducted to introduce large mass into single-chip gyroscopes (Park et al. 1999; Xie and Fedder 2002a). The single-chip approach can significantly cut down both the price and package size of MEMS gyroscopes, resulting in a much broader application range.

Complementary metal-oxide semiconductor (CMOS) processing has been the mainstream technology in the digital electronics world for about two decades. The enormous market volume of

[1] Assistant Professor, Dept. of Electrical and Computer Engineering, Univ. of Florida, Gainesville, FL 32611. E-mail: hkxie@ece.ufl.edu

[2] Professor, Dept. of Electrical and Computer Engineering, Carnegie Mellon Univ., Pittsburgh, PA 15213-3890. E-mail: fedder@ece.cmu.edu
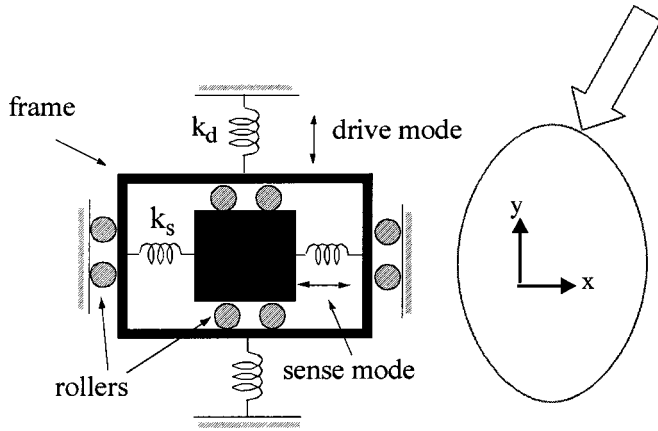
Fig. 1. Two-dimensional conceptual model of vibrating gimbaled gyroscope

digital electronics has supported the growth of foundries that specialize in CMOS processing and who continually improve the technology. Design compatibility of gyroscopes with conventional CMOS processes provides potential low cost due to the high availability and large market of CMOS.

This review focuses on vibratory-rate gyroscopes fabricated by single-chip integrated micromachining processes. First, the operational principle and design issues are introduced. Next, various micromachining processes are briefly described. Then, CMOS-compatible MEMS gyroscopes with different designs are reviewed, followed by a discussion of future trends.

Theory

Sensitivity, resolution, and stability are the primary performance measures of gyroscopes [IEEE Std 528-1994]. An analysis of these metrics for vibrating gyroscopes begins with the Coriolis phenomena. When a particle or structure moves in a rotating reference frame, this structure will experience a Coriolis force

$$\vec{F}_c = m\vec{a}_c \tag{1}$$

where m = mass of the structure. The corresponding Coriolis acceleration $\vec{a}_c$ is proportional to the velocity $\vec{v}$ of the moving structure and the rotation rate $\vec{\Omega}$ of the rotating reference frame.

$$\vec{a}_c = 2\vec{v} \times \vec{\Omega} \tag{2}$$

If the structure is suspended by a spring with a stiffness of k, the displacement $\vec{x}$ due to the Coriolis force is expressed as

$$\vec{x} = \frac{\vec{F}_c}{k} = \frac{m\vec{a}_c}{k} = \frac{\vec{a}_c}{\omega_r^2} \tag{3}$$

where $\omega_r = \sqrt{k/m}$ = resonant frequency.

Thus, from Eq. (3), a vibratory gyroscope is indeed an accelerometer. However, unlike accelerometers that detect translational motion, the accelerometer in a gyroscope must vibrate and the vibration velocity $\vec{V}$ must be known and stable in order to derive the rotation rate according to Eq. (2).

A simplified two-dimensional model of a vibrating gimbaled gyroscope is shown in Fig. 1. The suspensions provide appropriate elastic stiffness and constraints such that the central proof mass relative to the frame may only move in the x direction (sense mode) while the frame relative to the chip may only move

in the y direction (drive mode). The structure is a two-fold, orthogonal spring-mass-damper system with stiffness k_s and resonant frequency $\omega_{r,s}$ for the sense mode, and stiffness k_d and resonant frequency $\omega_{r,d}$ for the drive mode.

Suspended gyroscopes are usually underdamped, so the displacement amplitude, y, at the drive-mode resonance frequency, $\omega_{r,d}$, is amplified.

$$y = Q_d \frac{F_{dm}}{k_d} \sin \omega_{r,d}t \tag{4}$$

where F_{dm} = drive force amplitude; and Q_d = mechanical quality factor of the drive mode.

The vibrating drive motion in most micromachined gyroscopes is driven at resonance to take advantage of this amplification. The velocity v_y at resonance is

$$v_y = \dot{y} = Q_d \frac{F_{dm}\omega_{r,d}}{k_d} \cos \omega_{r,d}t \tag{5}$$

The second-order mechanical transfer function of the embedded sense accelerometer changes the magnitude and phase of the response given in Eq. (3), i.e., the displacement phasor is

$$|x| \angle \varphi_s = K_s \frac{|a_c|}{\omega_{r,s}^2} \angle \varphi_s = K_s \frac{2|v_y||\Omega_z|}{\omega_{r,s}^2} \angle \varphi_s \tag{6}$$

where Ω_z = rotation rate around the z axis,

$$K_s = \left[\left(1 - \left(\frac{\omega_{r,d}}{\omega_{r,s}} \right)^2 \right)^2 + \left(\frac{\omega_{r,d}}{Q_s\omega_{r,s}} \right)^2 \right]^{-1/2} \tag{7}$$

is the magnitude change relative to the quasistatic response,

$$\varphi_s = \tan^{-1}\left[\frac{\omega_{r,d}}{Q_s\omega_{r,s}} \left(1 - \left(\frac{\omega_{r,d}}{\omega_{r,s}} \right)^2 \right)^{-1} \right] \tag{8}$$

is the phase relative to the drive velocity and Q_s is the quality-factor of the sense mode. The drive frequency is chosen less than or equal to the accelerometer resonance, so the accelerometer signal is not attenuated. The two common design cases are $K_s \approx 1$, $\varphi_s \approx 0°$ when $\omega_{r,d} \ll \omega_{r,s}$, and $K_s = Q_s$, $\varphi_s \approx 90°$ when $\omega_{r,d} = \omega_{r,s}$.

Assuming a sinusoidal rotation signal $\Omega_z = \Omega_{zm} \cos(\omega_\Omega t)$ and substituting Eq. (5) into Eq. (6)

$$x(t) = K_s Q_d \frac{F_{dm}}{k_d} \frac{\omega_{r,d}\Omega_{zm}}{\omega_{r,s}^2} \{ \cos[(\omega_{r,d} - \omega_\Omega)t + \varphi_s]$$
$$+ \cos[(\omega_{r,d} + \omega_\Omega)t + \varphi_s] \} \tag{9}$$

where the magnitude term K_s and phase term φ_s are calculated assuming ω_Ω is negligible compared to $\omega_{r,d}$.

Eq. (9) shows that the mechanical sensitivity is determined by actuation amplitude, the drive and sense resonant frequencies, and the sense-mode quality factor (through K_s). Lowering the embedded accelerometer resonance frequency by increasing the proof mass leads to high-gyroscope sensitivity. The drive amplitude and resonance must be kept large for high sensitivity, so the drive voltage must be increased for larger proof mass. From Eq. (7), sensitivity is maximized when the two modes are exactly matched, but the bandwidth in this case is inversely proportional to the Q factor. Vacuum packaging can be used to increase both Q factors and thus the sensitivity. However, high-Q mechanical structures will ring with external disturbances, reducing the usable bandwidth and increasing the settling time of the gyroscope.

Eq. (9) also shows that the output is a modulated signal. An electronic demodulator is needed to recover the rotation signal. The modulation shifts the rotation signal from low frequency (0–300 Hz) to a much higher-frequency band, typically around 10 kHz, for accelerometer displacement. Therefore, translational acceleration with a frequency lower than the drive frequency can be rejected through filtering if the accelerometer has a linear response. If the accelerometer has a certain nonlinearity or limited linear range, external vibration noise will be mixed with the Coriolis signal (Xie 2002). In that case, differencing the signals from two matched antiphase gyroscopes, or from one gyroscope with two matched antiphase oscillating proof masses, will reject external translational acceleration.

Another important specification for a gyroscope is resolution or noise floor. The input-referred thermomechanical noise, or Brownian noise, of a gyroscope is given by

$$\frac{\Omega_{zm}}{\sqrt{BW}} = \sqrt{\frac{k_B T \omega_{r,s}}{m_s Q_s \omega_{r,d}^2 y_{dm}^2}} \quad (10)$$

where m_s = accelerometer proof mass; BW = gyroscope bandwidth; and $y_{dm} = Q_d F_{dm}/k_d$ = vibration amplitude of the drive mode. A typical surface micromachined gyroscope has parameters $m_s = 10$ μg, $Q_s = 100$, $\omega_{r,s} = \omega_{r,d} = 10$ kHz, and $y_{dm} = 5$ μm, leading to a Brownian noise of $0.03°/s/\sqrt{Hz}$. The thermomechanical noise spectral density, which is white, is integrated over the desired gyroscope bandwidth of around 300 Hz. As with the sensitivity, noise performance is improved by increasing the drive amplitude, drive resonance, and both Q factors, while decreasing the accelerometer resonant frequency.

The displacement due to Coriolis force is very small. The amplitude ratio of the sense motion and drive motion is obtained from Eq. (7), i.e.

$$\frac{x_{sm}}{y_{dm}} \bigg/ \Omega_{zm} = 2K_s \frac{\omega_{r,d}}{\omega_{r,s}^2} [°/s]^{-1} \quad (11)$$

For $K_s = 10$, and $\omega_{r,s} = \omega_{r,d} = 10$ kHz, this ratio is 6 ppm/°/s. Therefore, even a very small motion coupled from the drive mode will overwhelm the rotation signal. So, highly symmetric design and careful process tuning are required to minimize the coupling. There are two types of motion coupling: (1) quadrature and (2) direct motion coupling. Quadrature refers to the motion coupling that arises from anisoelasticity and other asymmetry. For example, suppose the gyroscope has driven motion in the y direction as assumed in the prior analysis. Due to the imperfections in the structure, small motions are coupled into the x and z directions too. The coupled x-axis motion is detected by the accelerometer and added to the Coriolis signal. The coupled motion is in phase with the primary drive motion. Therefore, since it is shifted in phase by 90° with respect to the Coriolis acceleration, the coupled motion is called quadrature or quadrature error [Clark et al. 1996]. This implies that the quadrature can be canceled out by properly tuning the phase of the carrier signal of the demodulator.

The second kind of coupling originates from the imperfections of the actuator. For example, interdigitated-finger "comb" drives are often used as electrostatic actuators. Due to process variations, there may be small geometric mismatches of a comb drive that create additional electrostatic forces in the cross-axis (x,z) directions. Typically, the structure is much stiffer in the two cross axes, and thus these direct motions are shifted in phase by ±90° with respect to the y-axis resonant motion. Since there is another 90° phase shift between the y-axis oscillation and the Coriolis acceleration [see Eq. (1)], the direct motion coupling has a 0° or 180°

phase shift from the Coriolis signal, implying that this direct motion coupling cannot be rejected by simply controlling the phase of the carrier of the demodulator (Xie et al. 2002b).

From Eq. (9), the output signal of the gyroscope is dependent on the drive amplitude and phase, the drive and sense resonance frequencies, and the accelerometer damping. All of these factors must be held constant, or the output will drift over time. In particular, the phase relationship at frequencies near resonance is very sensitive to small changes in these factors. For example, packaging stress can induce changes in spring constants, leading to changes in resonance frequency. All high-performance microgyroscopes require attention to packaging and closed-loop servo of amplitude and phase to null variations of this kind.

Integrated Micromechanical System Processes

Large sensitivity, low noise, selective mode matching and separation, undesired vibration coupling, and external translational acceleration rejection must be carefully considered during gyroscope design. Of prime importance is that the gyroscope designer must consider the structural imperfections due to material behavior and process variations, which affect these performance metrics.

Large proof mass, desirable for high sensitivity, is hard to realize in surface micromachining processes. Structural thickness is limited to around 10 μm for uniform thin-film deposition and structural area is limited to around 1 mm on a side to avoid problems with out-of-plane structural curling and with sticking to the substrate. However, wet etched bulk silicon gyroscopes have relatively large problems with spring and mass geometry control. Much better control of geometry is enabled with the advent of deep reactive-ion etching (DRIE) of silicon.

The capacitive sense interface circuit design is also a very challenging problem for both surface- and bulk-micromachined gyroscopes. Surface-micromachined gyroscopes have a typical sense capacitance of 0.1 pF. Bulk-micromachined gyroscopes normally have a relatively larger sense capacitance of 1 pF or greater, but most bulk silicon gyroscopes have not been integrated with electronics. The parasitic capacitance introduced by the wire bonding to electronic chips can greatly attenuate the signal. The dearth of integrated bulk silicon gyroscopes is partly due to the incompatibility of wet silicon through-wafer etching and wafer bonding with foundry electronics processes. The Si DRIE technology is still relatively new, and is expected to enable future generations of high-performance integrated microgyroscopes because of the ability to create precision bulk silicon structures directly in electronics processes.

For CMOS-compatible MEMS technology, micromachining steps can be performed before, after, or mixed with CMOS steps, namely, pre-CMOS, post-CMOS, and intra-CMOS micromachining, respectively (Baltes et al. 2002). Table 1 lists the comparison of these three types of process approaches. A CMOS-MEMS process may involve combinations of surface- and bulk-micromachining steps.

Pre-CMOS Micromachining

Pre-CMOS micromachining processes start with building MEMS structures on bare silicon wafers. Therefore, processing temperature can be high (>800°C), and thus the structures can be optimized to achieve excellent planarity. However, CMOS foundries

Table 1. Comparison of Complementary Metal-Oxide Semiconductor-Micromechanical System Processes

	Micromechanical system planarity	Temperature constraint for micromechanical system	Contamination constraint	Vendor accessibility
Pre-CMOS	Best	None	Yes	Limited
Intra-CMOS	Good	Yes	Yes	Very limited
Post-CMOS	Varies	yes	No	Good

will generally not accept such customized wafers, so a dedicated CMOS production line is required. A post-CMOS release step is also needed.

One example of pre-CMOS micromachining processes is the Sandia National Laboratories (SNL) IMEMS technology (Smith et al. 1995). The cross-sectional view of the process is shown in Fig. 2. Micromechanical devices are created within a shallow trench in the Si substrate, which is formed using an anisotropic etchant. Multiple layers of polysilicon and sacrificial silicon oxide are then deposited and patterned. Electrical contact between the microstructures and the CMOS electronics is made via polysilicon studs. Next, the shallow trenches are filled with silicon oxide, planarized with chemical-mechanical polishing (CMP) and annealed at high temperature to relieve stress in the structural polysilicon. At this point, the wafer is ready for conventional CMOS processing. After the CMOS processing is completed, a silicon nitride layer is deposited for the protection of the CMOS from wet HF of the final release step.

Intra-CMOS Micromachining

High-temperature annealing of certain microstructural materials, such as polysilicon, must be completed before the CMOS interconnect processing to avoid the melting temperature of the interconnect metals. The insertion of MEMS steps into the CMOS process steps posts potential compatibility problems with electronic doping that must be solved. This fully customized processing requires a dedicated production line.

A well-known example is Analog Devices, Inc.'s iMEMS technology (Core et al. 1993). The fabrication is based on a standard 24V 3μm BiCMOS process with trimable thin-film resistors. In this process, the deposition and annealing of structural materials is inserted prior to metallization. Si_3N_4 is used to protect the CMOS/BiCMOS area during the final wet etch release step. Fig. 3 shows the cross-sectional view. Compared to the pre-CMOS micromachining process shown in Fig. 2, no trench etch and CMP are needed in this process. However, after the structural layer is patterned, the wafer is not planar any more because the structural layer is typically a few microns above the rest of the wafer.

Consequently, only one interconnect layer may be feasible, and the electrical connection of the structural layer has to be the diffusion layer. Moreover, the influence of the high-temperature annealing to the performance of transistors must be considered when designing on-chip circuits.

Post-CMOS Micromachining

Post-CMOS micromachining processes build structures after completion of all conventional CMOS steps, enabling foundry production of the CMOS. Highly planar structures are more difficult to make, because processing temperatures must be under around 400°C so that the CMOS metallization does not melt. Contamination of the CMOS transistors from diffusion of MEMS materials is not an issue at such low temperatures.

Post-CMOS micromachining processes can be divided into two categories depending on how structural materials are made. One category is post-CMOS deposition, in which structural materials are deposited after standard CMOS processing. Another category is post-CMOS etching, in which microstructures are formed directly from the substrate and CMOS thin-film materials by etching.

Post-Complementary Metal-Oxide Semiconductor Deposition
Process temperatures for thin-film deposition and annealing must be lower than the melting point of the CMOS interconnect metal. Therefore, either high-temperature refractory metals are used or structural materials with low-deposition temperature and low stress must be found.

Researchers at University of California at Berkeley developed a Modular Integration of CMOS microStructures process using tungsten as the interconnect, $TiSi_2$ as the contact barrier, and Si_3Ni_4 for wet etch or vapor etch protection (Yun et al. 1992). However, high-temperature refractory metals have poor manufacturability and are not used as an interconnect in commercial CMOS processes. Recently, the same group proposed thin-film polycrystalline SiGe microstructures with low-deposition temperature to avoid the use of refractory interconnect metal (Franke 1999; Franke 2000). High-temperature annealing is not required
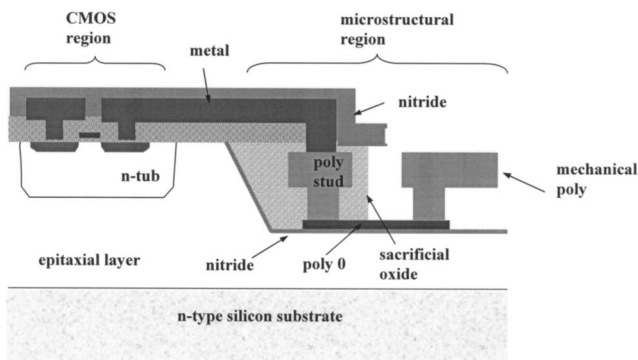
Fig. 2. Cross-section view of Sandia National Lab's iMEMS technology [Smith et al. 1995]
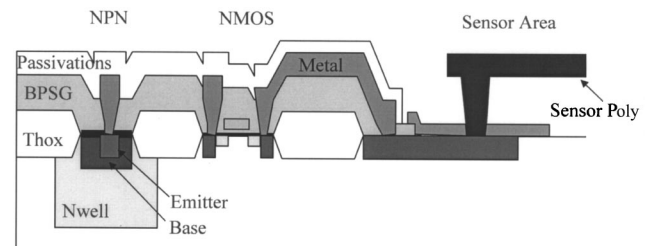
Fig. 3. Cross-section view of Analog Devices, Inc.'s iMEMS technology [Core et al. 1993]. Courtesy of John Geen.
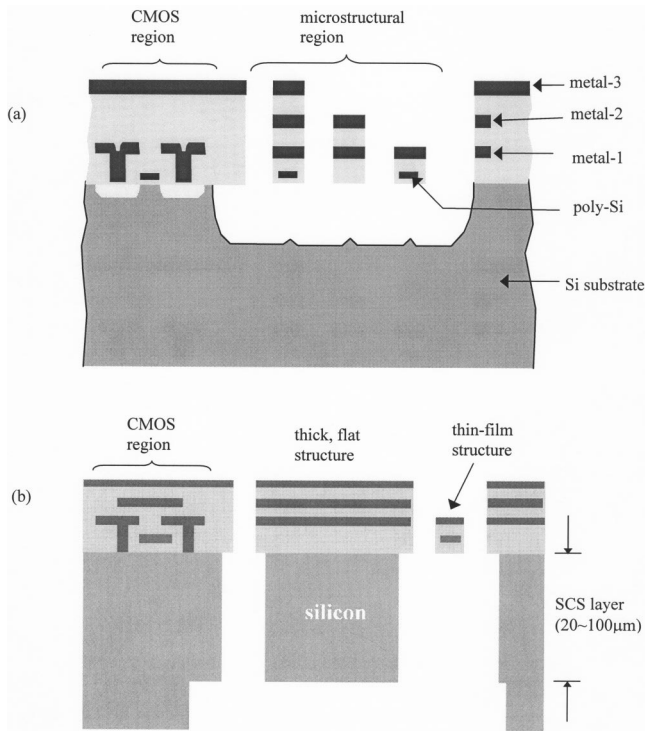
Fig. 4. Cross-sectional views of Carnegie Mellon CMOS-MEMS processes. (a) Thin-film process [Fedder et al. 1996]. (b) Backside etch process [Xie et al. 2002].

Fig. 5. Vibrating gyroscope topologies. Subscript d is drive mode, and subscript s is sense mode. (a) Single spring mass with translational drive. (b) Dual mass spring (tuning fork) with translational drive. (c) Single gimbaled mass with translational drive. (d) Single gimbaled mass with torsional drive. (e) Dual gimbaled mass with translational drive.
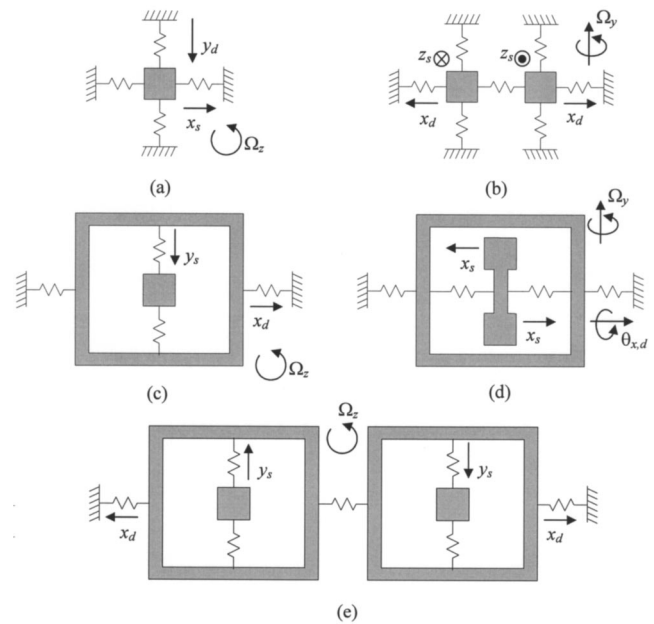
since the poly-SiGe structural layer has lower strain and strain gradient than poly-Si. In the process, poly-Ge, instead of oxide, is used as the sacrificial layer.

Delphi has developed electroplated metal structures on top of CMOS chips (Sparks et al. 1999). In the process, photoresist is used to form the mold and then a metal structure is electroplated at low temperature.

Post-Complementary Metal-Oxide Semiconductor Etching
In post-CMOS etching processes, microstructures are formed directly from the silicon substrate as well as the dielectric and metal layers normally used for interconnect. Baltes' group at ETH Zurich first used this approach to make CMOS sensors (Baltes et al. 1998). Wet silicon etching was employed to release microstructures.

Carnegie Mellon used a similar approach and developed two versions of CMOS-MEMS processes: thin-film and DRIE CMOS-MEMS processes [Fedder et al. 1996; Xie et al. 2002a]. Both post-CMOS processes involve only dry etch steps and use interconnect metal layers as etch masks. The process cross sections are shown in Fig. 4. When the chips come back from a CMOS vendor, the CMOS circuits are covered by the top metal and oxide, and the microstructures are predesigned by using the interconnect metal layers. The anisotropic dielectric etch is performed in a RIE etcher with a CHF_3/O_2 plasma. The deep silicon etch is performed by using the Bosch Advanced Silicon Etch process [Laermer and Schlip, U.S. Patent No. 5,501,893 (1996)] in a Surface Technology Systems system. The dry etch for release eliminates any sticking problems. Three-dimensional capacitive motion sensing and electrostatic actuation has been realized in both processes [Xie and Fedder 2002b; Xie et al. 2002a].

The main difference between the thin-film and DRIE CMOS-MEMS processes is that the latter incorporates single-crystal silicon (SCS) into mechanical structures by introducing a backside silicon etch into the process sequence. The SCS layer is typically about 60 μm thick. The cavity formed by the backside etch allows the completed die to be bonded directly to a package without interference from the released microstructures. As a final step, an optional timed isotropic Si etch may be performed. This step provides a specific undercut of bulk Si to create compliant structures or achieve electrical isolation of single-crystal silicon.

Integrated Micromechanical System Gyroscopes

Choice of topology is a critical step in gyroscope design. Vibrating gyroscopes may be categorized into single or dual spring mass or gimbaled mass, as summarized in Fig. 5. A single mass-spring system shares the same flexure for both the drive and sense modes, and thus suppressing mode coupling is a design issue. Dual mass structures can be arranged to form tuning fork resonators to reject transnational vibration. Single-gimbaled structures have an advantage of decoupling the drive and sense modes, but may have poor linear acceleration rejection and temperature performance. The dual-gimbaled structure in Fig. 5(e) is employed to improve the linear acceleration rejection and stability at the price of increased structural complexity.

Translational Vibration

Most vibrating microgyroscopes use translational actuation. In polysilicon processes, the movable part can be used as only one electrode, so both the drive comb and sense comb must have one electrode anchored on the substrate. MEMS processes that pro-
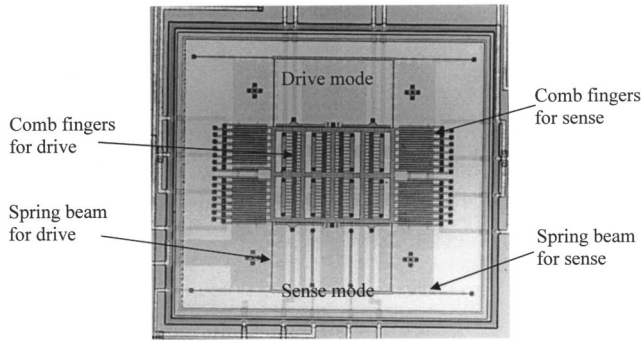
Fig. 6. A *z*-axis gyroscope fabricated using Analog Devices, Inc.'s iMEMS technology [Clark et al. 1996].

Fig. 8. Schematic and SEM of the mechanical structure of the resonant output gyroscope [Seshia et al. 2002].

vide multiple conducting layers have much higher-design flexibility, but the multiple layers of interconnect usually increases stress gradients in the structures.

Polysilicon Structures

Clark et al. demonstrated a *z*-axis gyroscope using ADI's iMEMS technology (Fig. 3) in 1996 (Clark et al. 1996). A scanning electron micrograph (SEM) of the device is shown in Fig. 6, where the sensor area is about 1 mm by 1 mm. The fixed-fixed flexure restricts motion to the *x* axis for the drive mode and to the *y* axis for the sense mode. The drive combs are located in the middle of the device, and the sense combs are on both sides to form a differential capacitance divider. Ideally, this capacitance pair compensates the capacitance changes in the drive direction and is only sensitive to the Coriolis motion in the orthogonal direction. On-chip circuits include a transresistance amplifier to detect the motional current from the capacitor divider and an integrator. The resonant frequency of the drive mode is about 12 kHz. Electrostatic frequency tuning of the sense mode was used to enhance sensitivity by matching drive and sense resonant frequencies. Quadrature error due to asymmetries in the vibrating structure was minimized electrostatically by controlling the voltages on the sense comb fingers. The measured noise floor was $1°/s/\sqrt{Hz}$.

Jiang et al. took further the advantage of the CMOS compatibility of the SNL IMEMS technology [Jiang et al. 2000]. A sigma-delta digital force-feedback circuit was integrated with the sensor. A SEM of the sensor structure is shown in Fig. 7. The sensor area is about 0.7 mm×0.8 mm, and the thickness of the mechanical structure is 2.25 μm. Parallel-plate actuation, instead
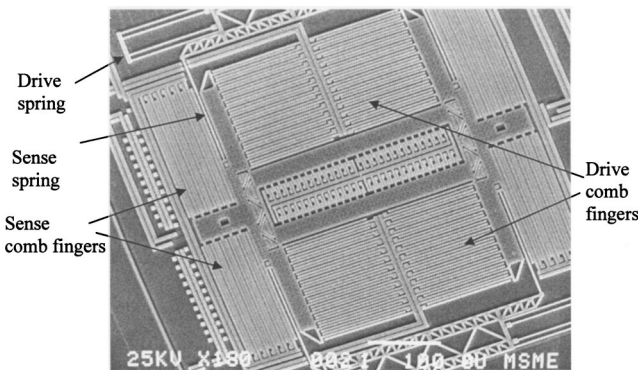
**Fig. 7.** SEM of a *z*-axis vibratory gyroscope with digital output [Jiang et al. 2000]. Courtesy of X. Jiang.
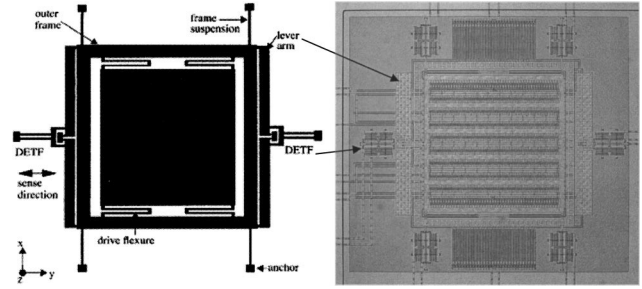
of commonly used longitudinal actuation, of comb drives was used for electrostatic actuation in this gyroscope design. The parallel-plate actuation provides larger electrostatic force for a given voltage at the expense of a limiting vibrational stroke. The drive comb fingers in the center are oriented 90° to the sense comb fingers on the two sides. Vibration amplitude of 1 μm was achieved with a 3 V drive voltage. The compliant suspension is similar to that of Clark's design shown in Fig. 6, but the whole structure is more compact and has higher area efficiency. A clock scheme was developed that decouples the drive and sense electronics. Offset, switch charge injection and other sampling errors, including kT/C noise were canceled using correlated double sampling in the switched-capacitor sense interface circuit. A noise floor of $3°/s/\sqrt{Hz}$ was measured at atmospheric pressure.

The two designs described above use capacitive bridges to measure the displacement induced by Coriolis force. Seshia et al. [Seshia et al. 2002] reported an integrated MEMS gyroscope based on resonant sensing. The schematic and SEM of this gyroscope design is shown in Fig. 8. The device was fabricated using the SNL IMEMS technology. The polysilicon sensor is about 1.2 mm by 1.2 mm in size and 2.25 μm thick. When there is an external rotation along the *z* axis, a Coriolis force induced by the vibration of the center proof mass acts on one end of a lever mechanism. The force is amplified by the lever and transmitted to a double-ended tuning fork (DETF) along the axial direction of the DETF. The resonant frequency of the DETF is sensitive to axial stress. Therefore, the DETF self-oscillation frequency is a measure of the external rotation rate.

There is one DETF on either side of the structure to form a differential output. The output of the gyroscope is a frequency-modulated signal that can be easily converted to a digital signal. Note that it is the proof mass, not the outer frame, that was driven to oscillation in the *x* direction during the operation of this device. The measured noise floor is $0.3°/s/\sqrt{Hz}$, limited by electronic noise of the oscillator circuit.

The single-resonator gyroscope designs discussed above are prone to environmental vibrations. Geen et al. [Geen et al. 2002] reported a dual-resonator *z*-axis gyroscope fabricated using ADI's iMEMS technology with 4 μm-thick structural polysilicon. As shown in Fig. 9, the sensor consists of two identical resonators driven with equal amplitude in opposite directions. The differential output of the two Coriolis signals effectively rejects external linear acceleration. On-chip electronics include circuits for self-oscillation, phase control, demodulation, and temperature compensation. A unique controlled-impedance field-effect transistor is used to bias the input (the capacitive sense node) of the transresistance pre-amplifier. The bias transistor provides an equivalent resistance of 2.5 GΩ. The resonance frequency of the drive mode
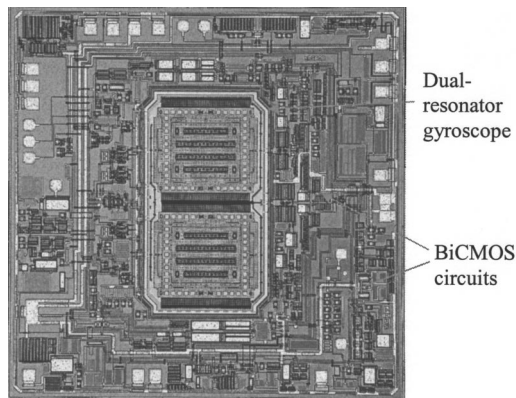
**Fig. 9.** Micrograph of ADI dual-resonator gyroscope [Geen et al. 2002]. Courtesy of John Geen.

is 15 kHz with a mechanical Q of about 45, leading to a 10 μm peak-peak drive displacement generated with 12 Vac. The measured noise floor of the device is $0.05°/s/\sqrt{Hz}$.

Multilayer Thin-Film Structures

The CMOS-MEMS process shown in Fig. 4(a) provides structures with multiple conducting layers isolated by dielectrics, eliminating the electrical isolation constraint existing in most other MEMS processes. Thus, elastically gimbaled structures with decoupled sense and drive modes can be realized. Both lateral-axis and z-axis gyroscopes have been demonstrated [Xie and Fedder 2001; Luo et al. 2002].

The gimbaled lateral-axis gyroscope shown in Fig. 10 was fabricated by a thin-film CMOS micromachining, starting with Agilent 0.5 μm three-metal CMOS (Xie and Fedder 2001). The microstructure is 5 μm thick and 0.8 mm by 0.6 mm in size. The central y-axis accelerometer is anchored on a rigid frame. The rigid frame is connected to the substrate via a flexure that is compliant in the z direction. A z-axis comb drive is employed, so that the embedded accelerometer is driven in vertical oscillation, and x-axis rotation is then detected.

The out-of-plane curling of the drive spring beams is due to the residual stress and thermal expansion coefficient difference of the materials in the beams. An on-chip buffer circuit detects the motional capacitance of the accelerometer. The on-chip buffer has low-parasitic capacitance, so input attenuation of the motional signal is minimal. The resonant frequency of the drive mode is 5
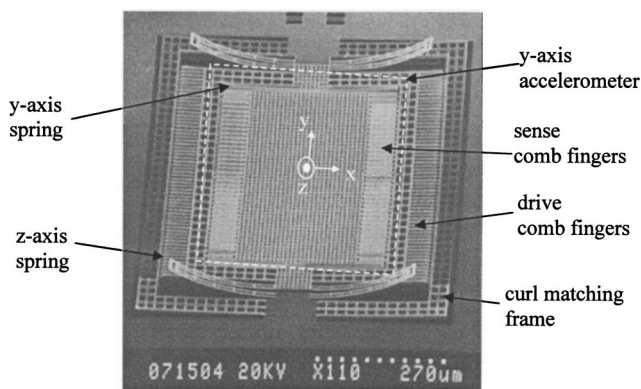
Fig. 10. SEM of integrated x-axis gyroscope fabricated by a thin-film CMOS-MEMS process [Xie and Fedder 2001]
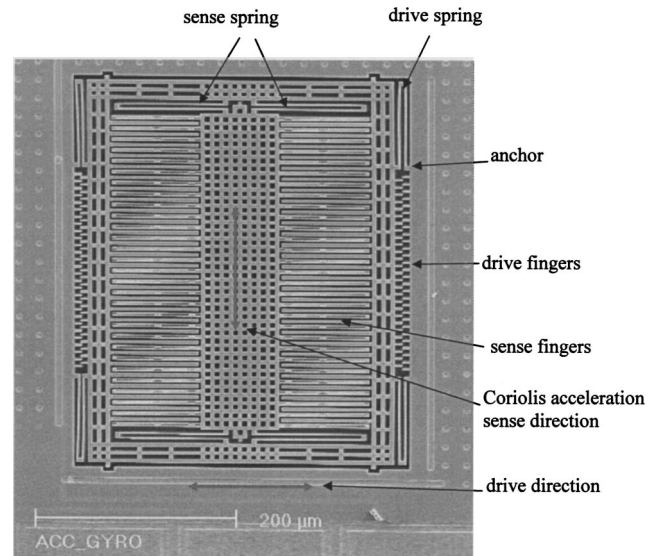
Fig. 11. SEM of integrated z-axis gyroscope fabricated by a thin-film CMOS-MEMS process [Luo et al. 2002]. Courtesy of H. Luo.

kHz, and matching to the sense-mode resonance was achieved using thermomechanical tuning of the springs. The noise floor of the sensor at atmospheric pressure is $0.5°/s/\sqrt{Hz}$, limited by electronics noise.

Luo et al. demonstrated a z-axis integrated gyroscope by CMOS micromachining, starting with UMC 0.18 μm six-copper layer CMOS (Luo 2002). Fig. 11 shows a SEM of the mechanical structure of a fabricated device. The thickness of the structure is about 8 μm with a sensor area of 410 μm×330 μm. Though its topology is similar to the one shown in Fig. 10, this z-axis gyroscope employs in-plane comb drives for both excitation and Coriolis acceleration sensing. The resonant frequency of the drive mode is 8.8 kHz. The device operates at the atmospheric pressure and a noise floor of $0.5°/s/\sqrt{Hz}$ was achieved.

Combining the above two types of gyroscopes can directly result in single-chip integrated three-axis gyroscopes. The main issues of this type of thin-film CMOS-MEMS gyroscopes include size limitation due to curling, and strong temperature dependence of multilayer structures.

Combined Single-Crystal Silicon and Thin-Film Structures

MEMS processes with the ability to create both SCS and thin-film microstructures provide flatness and large mass as well as three-axis compliance and three-axis actuation.

The writers fabricated a bulk silicon vibratory gyroscope [Xie and Fedder 2002a] using a DRIE CMOS-MEMS process that uses Austria Microsystems three-metal 0.6 μm CMOS. Fig. 12 is a SEM of a released device, which is a lateral-axis angular rate sensor with in-plane vibration and out-of-plane Coriolis acceleration sensing. The sensor plus on-chip CMOS circuitry is 1 mm by 1 mm in size. It incorporates both 1.8 μm-thick thin-film structures for spring beams with out-of-plane compliance and 60 μm-thick bulk Si structures for spring beams with in-plane compliance. The microstructure is flat because of the underlying thick silicon layer and thereby avoids potential curling problems, which exist in some thin-film CMOS-MEMS gyroscopes. A unique silicon electrical isolation technique is used to obtain individually controllable comb fingers [Xie et al. 2002a]. The noise floor of

comb fingers for vibration control

sense spring

drive comb fingers

drive spring

sense comb fingers
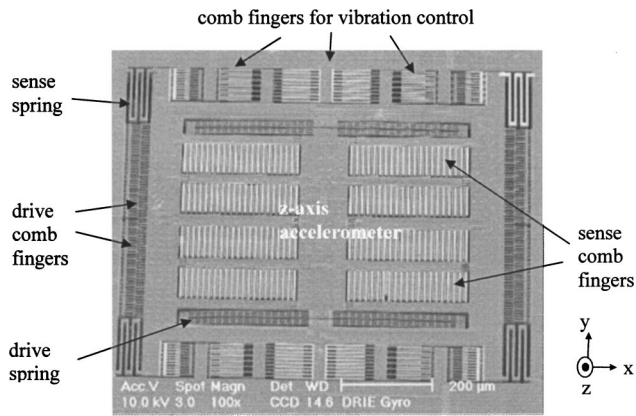
Fig. 12. SEM of DRIE x-axis gyroscope fabricated by Carnegie Mellon DRIE CMOS-MEMS process [Xie and Fedder 2002a]

the gyroscope is $0.02°/s/\sqrt{Hz}$ at 5 Hz. The resolution of this DRIE gyroscope is one order of magnitude higher than that of thin-film counterparts.
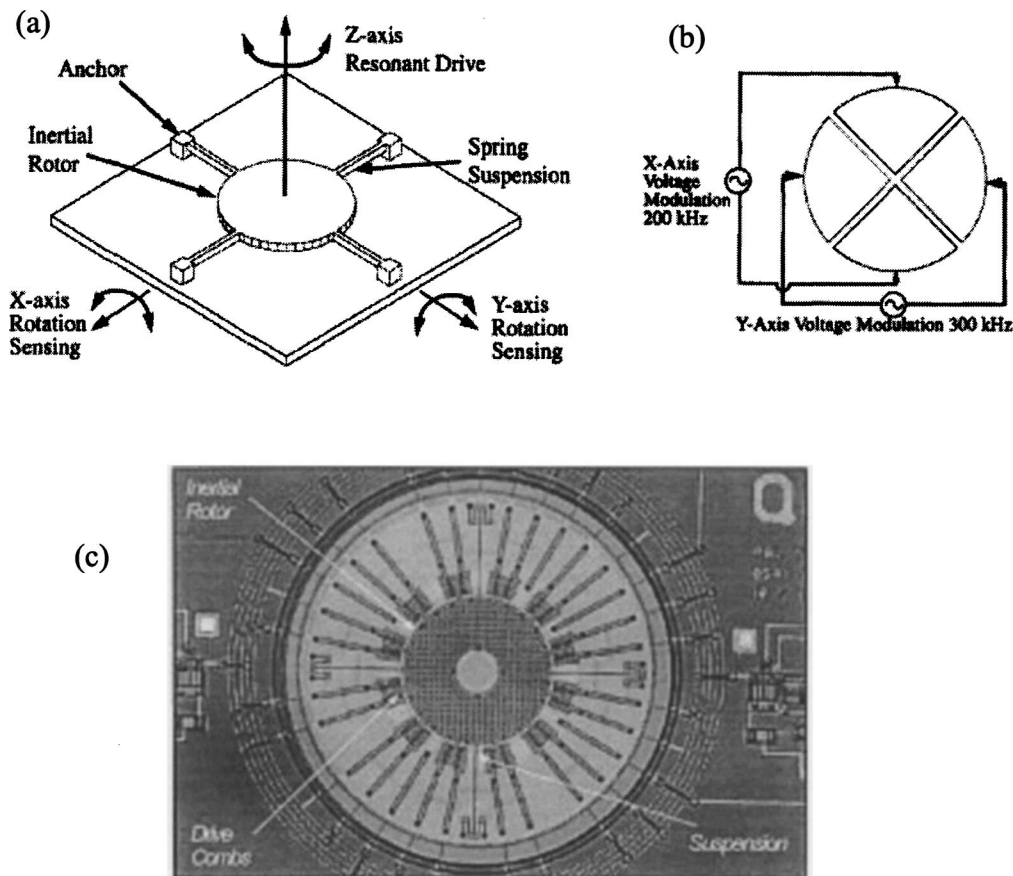
Rotational Vibration

Rotational vibration around the z-axis makes it possible to detect lateral-axis angular rate with out-of-plane Coriolis acceleration sensing. Juneau et al. reported a dual axis gyroscope with a quad symmetry of a circular oscillating rotor design in the SNL iMEMS technology [Juneau et al. 1997]. As shown in Fig. 13(a), the inertial rotor is suspended by four beams, which are anchored to the substrate and provide torsional compliance about all three axes. The rotor has a diameter of 300 μm and is made of 2-μm-thick polysilicon with a 1.6 μm gap to the substrate. The rotor is surrounded by radial electrostatic comb drives, which generate the torsional oscillation along the z axis. When an external rotation exists around the x or y axis, the rotor will tilt along the y or x axis, respectively, according to Eq. (1). Two pairs of parallel-plate capacitance electrodes are placed underneath the rotor by $n+$ diffusion in the substrate, with the rotor used as a common output electrode. Thus, two sets of differential capacitive bridges are formed. One set measures the x axis tilt and the other set measures the y axis tilt. Since the rotor is a single electrode, the signals for both axes share the same signal node. In order to distinguish the two axis signals, two different modulation frequencies are applied, as shown in Fig. 13(b).

A SEM of a fabricated device is shown Fig. 13(c). The suspension beams were designed to match the resonant frequency of 28 kHz in all three axes. Additional electrostatic tuning was also used to obtain better mode matching. The device achieved $0.3°/s/\sqrt{Hz}$ noise floor with cross sensitivity as much as 16% under open-loop conditions. A close-loop force balancing control scheme was proposed to reduce cross sensitivity and cancel quadrature error.

Bosch also reported a thick-polysilicon lateral-axis gyroscope with torsional actuation [Funk et al. 1999]. However, the fabrication process is not compatible with CMOS processing.

Fig. 13. Dual-axis integrated gyroscope [Juneau et al. 1997]. (a) Schematic; (b) modulation signals; and (c) micrograph of a fabricated device.
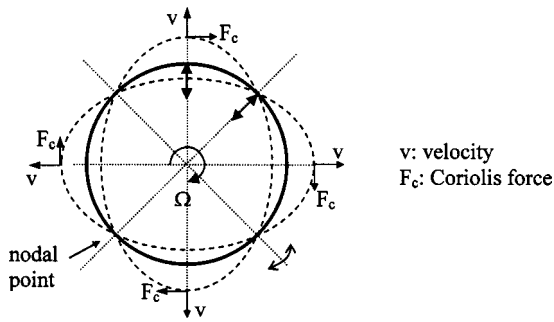
Fig. 14. Operational principle of a ring gyroscope

Vibrating Ring Gyroscope

In a vibrating ring gyroscope [Putty and Najafi 1994; Sparks et al. 1999], the ring structure is driven into resonance in the plane of the chip. The vibration of the ring forms an elliptically shaped pattern. In the absence of an external rotation, the four nodal points at $+/-$ 45° from the drive axis on the ring remain stationary, as shown in Fig. 14. An external rotation about the z axis generates a Coriolis force that excites the resonant mode along the 45° axes. The resulting displacement is sensed capacitively by a series of electrodes around the ring. The symmetry of the structure provides identical drive and sense resonance if manufacturing is perfect.

Delphi reported a vibratory ring gyroscope using electroplated metal to form a ring structure on top of CMOS chips [Sparks et al. 1999]. A SEM of the device is shown in Fig. 15. Semicircular springs support the ring and store the vibration energy. The springs are attached to the substrate with a symmetric post. The post/spring design greatly reduces the effect of packaging stresses on the sensor. Electrodes with a small gap to the ring are placed along the circumference of the ring with equal intervals. These electrodes, forming capacitors with the ring, are used to drive, sense, balance, and control the ring vibration. During operation, an ac voltage signal is applied to the drive electrodes to excite the ring electrostatically into resonant oscillation. A dc bias voltage is applied to the ring. The sense electrodes are 45° apart from the corresponding drive electrodes and are connected to on-chip low-input-capacitance CMOS buffer amplifiers. Another ASIC chip that includes four independent control loops is used to maintain the ring in resonance at a constant amplitude, to obtain the rate signal, and to correct for mechanical imbalance in the ring. The sensor has a measured noise floor of $0.1°/s/\sqrt{Hz}$ and a bandwidth of 25 Hz.
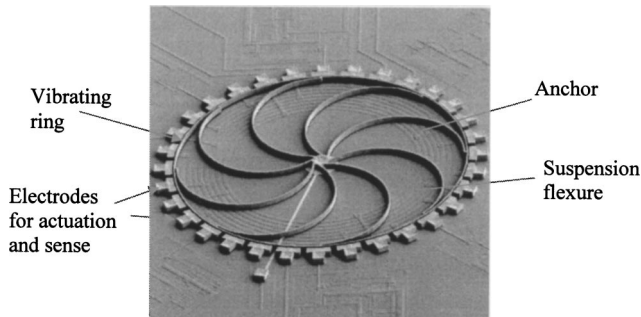

Fig. 15. Delphi's metal ring gyroscope [Sparks et al. 1999]

Summary and Future Trends

There are various structural topologies for vibrating gyroscopes. Dual-resonator and ring structures have good vibration rejection and temperature performance. Translationally vibrating structures can be designed to sense both lateral-axis and vertical-axis rotation. Torsionally vibrating structures provide lateral-axis angular rate detection. The choice of a topology for a gyroscope strongly depends on the capability of the available fabrication process.

Pre-CMOS, intra-CMOS, and post-CMOS micromachining processes have their advantages and disadvantages. Pre-CMOS and inter-CMOS processes require a dedicated production line and thus require a large engineering investment. Post-CMOS micromachining processes provide high accessibility and much lower cost. The key for post-CMOS micromachining processes is how to form and process the structural materials. Polysilicon is the most popular and most explored material for pre- and intra-CMOS micromachining processes. However, it cannot be adopted into post-CMOS micromachining processes because of the temperature constraint. Alternative materials such as low-deposition temperature SiGe or electroplating metals have been studied and have very high potential for future gyroscopes.

The post-CMOS etching of MEMS approach is a relatively simple process and thus can produce inexpensive integrated MEMS devices by using the materials directly from CMOS processing. The temperature performance is a major concern for microstructures made of only metal and dielectric materials. However, microstructures with combined single-crystal silicon and metal/dielectric layers are flat and have electrical isolation and good temperature stability, allowing their potential application in future gyroscopes.

Analog Devices just launched the first commercially available integrated MEMS gyroscope in October 2002. Though time is needed to see how markets evolve, the small size, ease of use, and relatively low cost of the integrated gyroscope is expected to open new application areas. Nevertheless, technology development is still needed to improve the CMOS compatibility to further reduce the price. Microgyroscope resolution and stability needs to be improved to broaden the range of applications. In particular, the bias stability of current micromachined gyroscopes is not able to meet navigation-grade specifications.

Multiple-axis integration is important to reduce the overall package size and cost. The integration of electronics is not limited to interface, signal conditioning, and analog-to-digital circuitry. The CMOS compatibility assures the possibility of adding as much circuits as needed. Self-powered, single-chip gyroscopes plus accelerometers with wireless communications are ultimately possible. The applications then will not just be in automobiles, computer games or space navigation systems, but widespread in consumer electronics and appliances.

References

Ayazi, F., and Najafi, K. (2001). "A HARPSS polysilicon vibrating ring gyroscope." *J. Microelectromech. Syst.,* 10(2), 169–179.

Baltes, H., Brand, O., Hierlemann, A., Lange, D., and Hagleitner, C. (2002). "CMOS MEMS—Present and future." *Proc., The Fifteenth IEEE Int. Conf. on Micro Electro Mechanical Systems (MEMS 2002)*, Las Vegas, Jan. 20–24, 459–466.

Baltes, H., Paul, O., and Brand, O. (1998). "Micromachined thermally based CMOS microsensors." *Proc. IEEE,* 86(8), 1660–1678.

Bernstein, J., Cho, S., King, A. T., Kourepenis, A., Maciel, P., and Weinberg, M. (1993). "A micromachined comb-drive tuning fork rate gy-

roscope.'' *Proc., 6th IEEE Int. Conf. on Microelectromechanical Systems*, Fort Lauderdale, Fla., Feb. 7–10, 143–148.

Clark, W. A., Howe, R. T., and Horowitz, R. (1996). "Surface micromachined Z-axis vibratory rate gyroscope." *Technical Digest. Solid-State Sensor and Actuator Workshop*, Hilton Head Island, S.C., June 3–6, Transducers Research Found., 283–287.

Core, T. A., Tsang, W. K., and Sherman, S. J. (1993). "Fabrication technology for an integrated surface-micromachined sensor." *Solid State Technol.,* 36(10), 39–47.

Fedder, G. K., Santhanam, S., Reed, M. L., Eagle, S. C., Guillou, D. F., Lu, M. S.-C., and Carley, L. R. (1996). "Laminated high-aspect-ratio microstructures in a conventional CMOS process." *Sens. Actuators A,* A57(2), 103–110.

Franke, A. E., Bilic, D., Chang, D. T., Jones, P. T., King, T.-J., Howe, R. T., and Johnson, G. C. (1999). "Post-CMOS integration of germanium microstructures." *Proc., Twelfth IEEE Int. Conf. on Micro Electro Mechanical Systems (MEMS '99)*, Orlando, Fla., Jan. 17–21, 630–637.

Franke, A. E., Jiao, Y., Wu, M. T., King, T.-J., and Howe, R. T. (2000). "Post-CMOS modular integration of poly-SiGe microstructures using poly-Ge sacrificial layers." *Technical Digest IEEE Solid-State Sensor & Actuator Workshop*, Hilton Head Island, S.C., June 4–8, Transducers Research Found., 18–21.

Funk, K., Emmerich, H., Schilp, A., Offenberg, M., Neul, R., and Larmer, F. (1999). "A surface micromachined silicon gyroscope using a thick polysilicon layer." *Proc., Twelfth IEEE Int. Conf. on Micro Electro Mechanical Systems (MEMS '99)*, Jan. 17–21, Orlando, Fla., 57–60.

Geen, J. A., Sherman, S. J., Chang, J. F., and Lewis, S. R. (2002). "Single-chip surface-micromachining integrated gyroscope with 50 deg/hour root Allan variance." *Digest of 2002 IEEE International Solid-State Circuits Conference*, San Francisco Feb. 3–7, 426–427.

Greiff, P., Boxenhorn, B., King, T., and Niles, L. (1991). "Silicon monolithic micromechanical gyroscope." *Proc., IEEE 1991 Int. Conf. on Solid State Sensors and Actuators*, San Francisco, June 24–27, 966–968.

He, G., and Najafi, K. (2002). "A single-crystal silicon vibrating ring gyroscope." *Proc., The Fifteenth IEEE Int. Conf. on Micro Electro Mechanical Systems (MEMS 2002)*, Las Vegas, Jan. 20–24, 718–721.

Hombersley, S. (2002). "BAE Systems and Segway LLC announce partnership to market Segway™ human transporter in the UK." ⟨http://www.baesystems.com/newsroom/2002/jul/220702news8.htm⟩ (July 22, 2002).

Hopkin, I. D. (1994). "Vibrating gyroscopes (automotive sensors)." *IEEE Colloquium on 'Automative Sensors'* (Digest No. 1994/170), Sept. 13, Solihull, UK, 1–4.

IEEE Std 528-1994. (1994). "IEEE standard for inertial sensor technology." The Institute of Electrical and Electronics Engineers, Inc., New York.

Jiang, X., Seeger, J. I., Kraft, M., and Boser, B. E. (2000). "A monolithic surface micromachined Z-axis gyroscope with digital output." *Digest of Technical Papers, 2000 Symposium on VLSI Circuits*, June 15–17, Honolulu, 16–19.

Juneau, T., Pisano, A. P., and Smith, J. H. (1997). "Dual axis operation of a micromachined rate gyroscope." *Proc., IEEE 1997 Int. Conf. on Solid State Sensors and Actuators (Tranducers '97)*, Chicago, June 16–19, 883–886.

Kurosawa, M., Fukuda, Y., Takasaki, M., and Higuchi, T. (1998). "A surface-acoustic-wave gyro sensor." *Sens. Actuators A,* A66(1–3), 33–39.

Luo, H., Zhu, X., Lakdawala, H., Carley, L. R., and Fedder, G. K. (2002). "A copper CMOS-MEMS z-axis gyroscope." *Proc., The Fifteenth IEEE Int. Conf. on Micro Electro Mechanical Systems (MEMS 2002)*, Las Vegas, Jan. 21–25, 631–634.

Lutz, M., Golderer, W., Gerstenmeier, J., Marek, J., Maihofer, B., Mahler, S., Munzel, H. and Bischof, U. (1997). "A precision Yaw Rate Sensor in Silicon Micromachining." *Proc., IEEE 1997 Int. Conf. on Solid State Sensors and Actuators*, Chicago, June 16–19, 847–850.

Maenaka, T., Konishi, K., Fujita, Y., and Maeda, M. (1995). "Analysis of a highly sensitive silicon gyroscope with cantilever beam as vibrating mass." *Digest, The Eighth IEEE Int. Conf. on Solid-State Sensors and Actuators and Eurosensors IX*. June 25–29, Stockholm, Sweden, 612–615.

Mochida, Y., Tamura, M., and Ohwada, K. (1999). "A micromachined vibrating rate gyroscope with independent beams for the drive and detection modes." *Proc., Twelfth IEEE Int. Conf. on Micro Electro Mechanical Systems (MEMS '99)*, Orlando, Fla., Jan. 17–21, 618–623.

Park, K. Y., Jeong, H. S., An, S., Shin, S. H., and Lee, C. W. (1999). "Lateral gyroscope suspended by two gimbals through high aspect ratio ICP etching." *Proc., IEEE 1999 Int. Conf. on Solid State Sensors and Actuators (Tranducers '99)*, Sendai, Japan, June 7–10, 972–975.

Park, K. Y., Lee, C. W., Oh, Y. S., and Cho, Y. H. (1997). "Laterally oscillated and force-balanced micro vibratory rate gyroscope supported by fish hook shape springs." *Proc., Tenth IEEE Int. Conf. on Micro Electro Mechanical Systems (MEMS '97)*, Nagoya, Japan, Jan. 26–30, 494–499.

Payne, R. S., Sherman, S., Lewis, S., and Howe, R. T. (1995). "Surface micromachining: From vision to reality to vision (accelerometer)." *Digest of Technical Papers, 1995 IEEE Int. Solid-State Circuits Conf. (ISSCC '95)*, Feb. 15–17, San Francisco, 164–165.

Putty, M. W., and Najafi, K. (1994). "A micromachined vibrating ring gyroscope." *Technical Digest, Solid-State Sensor and Actuator Workshop*, Hilton Head Island, S.C., June 13–16, Transducers Research Found., 213–220.

Seshia, A. A., Howe, R. T., and Montague, S. (2002). "An integrated microelectromechanical resonant output gyroscope." *Proc., The Fifteenth IEEE Int. Conf. on Micro Electro Mechanical Systems (MEMS 2002)*, Las Vegas, Jan. 21–25, 722–726.

Shearwood, C., Williams, C. B., Mellor, P. H., Yates, R. B., Gibbs, M. R. J., and Mattingley, A. D. (1995). "Levitation of a micromachined rotor for application in a rotating gyroscope," *Electron. Lett.,* 31(21), 1845–1846.

Smith, J. H., Montague, S., Sniegowski, J. J., and Murray, J. R. et al. (1995). "Embedded micromechanical devices for the monolithic integration of MEMS with CMOS." *Proc., Int. Electron Devices Meeting*, Washinton, DC, Dec. 10–13, 609–619.

Sparks, D., Slaughter, D., Beni, R., Jordan, L., Chia, M., Rich, D., Johnson, J., and Vas, T. (1999). "Chip-scale packaging of a gyroscope using wafer bonding," *Sens. Mater.,* 11(4), 97–207.

Tanaka, K., Mochida, Y., Sugimoto, S., Moriya, K., Hasegawa, T., Atsuchi, K., and Ohwada, K. (1995). "A micromachined vibrating gyroscope," *Proc., Eighth IEEE Int. Conf. on Micro Electro Mechanical Systems (MEMS '95)*, Amsterdam, Netherlands; 29 Jan.–2 Feb., 278–281.

Tang, T. K., Gutierrez, R. C., Stell, C. B., Vorperian, V., Arakaki, G. A., Rice, J. T., Li, W. J., Chakraborty, I., Shcheglov, K., Wilcox, J. Z., and Kaiser, W. J. (1997). "A packaged silicon MEMS vibratory gyroscope for microspacecraft." *Proc., Tenth IEEE Int. Conf. on Micro Electro Mechanical Systems (MEMS '97)*, Nagoya, Japan, Jan. 26–30, 500–505.

Wisniowski H. (2002). "Analog Devices introduces world's first integrated gyroscope." ⟨http://www.analog.com/technology/mems/gyroscopes⟩ (October 1, 2002).

Xie, H. (2002). "Gyroscope and Micromirror Design Using Vertical-Axis CMOS-MEMS Actuation and Sensing." PhD thesis, Carnegie Mellon Univ., Pittsburgh, Pa., 2002.

Xie, H., Erdmann, L., Zhu, X., Gabriel, K., and Fedder, G. K. (2002a). "Post-CMOS Processing For High-aspect-ratio Integrated Silicon Microstructures." *J. Microelectromech. Syst.,* 11(2), 93–101.

Xie, H., and Fedder, G. K. (2001). "A CMOS-MEMS Lateral-axis Gyroscope." *Proc., The Fourteenth IEEE Int. Conf. on Micro Electro Mechanical Systems (MEMS 2001)*, Interlaken, Switzerland, January 21–25, 162–165.

Xie, H., and Fedder, G. K. (2002a). "A DRIE CMOS-MEMS

Gyroscope.'' *IEEE Sensors 2002 Conf.* June 12–14, Orlando, Fla.

Xie, H., and Fedder, G. K. (2002b). ''Vertical Comb-finger Capacitive Actuation and Sensing for CMOS-MEMS,'' *Sens. Actuators A,* A95(2–3), 212–221.

Xie, H., Fedder, G. K., Pan, Z., and Frey, W. (2002b). ''Phase and vibration analysis for a CMOS-MEMS gyroscope.'' *Int. J. Nonlinear Sci-*

ences Numerical Simulation, 3(3–4), 319–324.

Yun, W., Howe, R. T., and Gray, P. R. (1992). ''Surface micromachined, digitally force-balanced accelerometer with integrated CMOS detection circuitry.'' *Technical Digest IEEE Solid-State Sensor & Actuator Workshop*, Hilton Head Island, S.C., June 22–25, Transducer Research Foundation, 126–131.